

Spin-resolved Andreev levels in hybrid superconductor-semiconductor nanostructures

Eduardo J. H. Lee¹, Xiaocheng Jiang², Manuel Houzet¹, RamónAguado³, Charles M. Lieber², and Silvano De Franceschi^{1*}¹*SPSMS, CEA-INAC/UJF-Grenoble 1, 17 rue des Martyrs, 38054 Grenoble Cedex 9, France*²*Harvard University, Department of Chemistry and Chemical Biology, Cambridge, MA, 02138, USA and*³*Instituto de Ciencia de Materiales de Madrid (ICMM),**Consejo Superior de Investigaciones Científicas (CSIC),**Sor Juana Inés de la Cruz 3, 28049 Madrid, Spain*

(Dated: March 4, 2019)

The combination of superconductors and low-dimensional conductors embodies a rich, yet largely unexplored physics. In this hybrid system, macroscopic properties enforced by superconductivity can be controlled through electrically tunable microscopic degrees of freedom, inherent to a relatively small number of confined electrons [1–8]. Here we consider the prototypical case of a quantum dot (QD) coupled strongly to a superconductor (S) and weakly to a normal-metal (N) tunnel probe. We investigate the magnetic properties of the lowest-energy, sub-gap states, which are governed by a competition between superconducting pairing and Coulomb repulsion [2, 3, 9–13]. In a magnetic field, only when the ground state is a spin singlet, can the Zeeman splitting of the (excited) doublet be revealed by tunnel spectroscopy. The splitting is strongly influenced by a level-repulsion effect with the continuum of quasi-particle states; and it can induce a quantum phase transition (QPT) to a spin-polarized state. Our experimental results, supported by theory, hold relevance for current research on quantum-information devices [14, 15] and Majorana fermions in hybrid nanostructures [16–20].

QDs coupled to S electrodes can be seen as artificial realizations of quantum impurity systems, a core problem in the physics of strongly correlated electron systems. In the QD- S system, superconducting pairing correlations favour the mixing of evenly-occupied charge states of the QD. Under the simplest assumption of a QD with a single spin-degenerate orbital level, four eigenstates are possible: a spin-degenerate magnetic doublet ($|\uparrow\rangle, |\downarrow\rangle$), and two BCS-like singlets ($|- \rangle = -v^*|\uparrow\downarrow\rangle + u|0\rangle$, and $|+ \rangle = u|\uparrow\downarrow\rangle + v^*|0\rangle$) [10, 13]. For odd occupation, the magnetic doublet, favoured by the on-site Coulomb interaction, and the $|- \rangle$ state, favoured by superconducting pairing, compete for being the ground state (GS), whereas $|+ \rangle$ always lies at higher energies. This competition is governed by the interplay of different energy scales: the charging energy, U , the superconducting gap, Δ , the QD- S tunnel coupling, Γ_S , responsible for quantum fluctuations in the QD charge, and the energy ϵ_0 of

the QD level relative to the Fermi energy of the S electrode (see Fig. 1a) [2, 3, 9–13]. The qualitative phase diagram in the lower part of Fig. 1a shows that for sufficiently large Γ_S/U the QD stays always in the singlet GS.

Here we investigate the magnetic properties of the lowest-energy states in a S -QD- N geometry, where the N contact acts as a weakly coupled tunnel probe. In this geometry, a measurement of the differential conductance, dI/dV , as a function of the source-drain voltage, V , enables a direct spectroscopy of the density of states (DOS) in the QD- S system. In such a measurement, the flow of an electrical current involves single-electron fluctuations in the QD charge. At low energy, these charge fluctuations correspond to elementary excitations between the GS and the first excited state (ES), namely between ($|\uparrow\rangle, |\downarrow\rangle$) and $|- \rangle$, or vice-versa. As a result, sub-gap resonances in dI/dV appear at $eV = \pm|\zeta|$, where ζ is the excitation energy (see Fig. 1a) [21–24]. These sub-gap resonances, often referred to as Andreev levels, are responsible for the Josephson effect in S -QD- S devices.

We used devices based on single InAs/InP core/shell nanowires (NWs), where vanadium (gold) was used for the S (N) contact [25]. A device schematic and a representative image are shown in Figs. 1c and 1d, respectively. The fabricated vanadium electrodes showed $\Delta = 0.55$ meV and an in-plane critical magnetic field $B_c^x \approx 2$ T ($x \parallel$ NW axis). The QD is naturally formed in the NW section between the S and N contacts. We find typical U values of a few meV (i.e., $U/\Delta \approx 3 - 10$). The QD properties are controlled by means of two bottom electrodes crossing the NW, labeled as plunger gate and S -barrier gate, and a back gate provided by the conducting Si substrate. To achieve the asymmetry condition $\Gamma_S \gg \Gamma_N$, the S -barrier gate was positively biased at $V_{sg} = 2$ V. We used the plunger gate voltage V_{pg} to vary the charge on the QD, and the back-gate voltage V_{bg} to finely tune the tunnel coupling.

Figure 2a shows a series of $dI/dV(V_{pg}, V)$ measurements for three different Γ_S . The top row refers to the weakest Γ_S . In this case, the spanned V_{pg} range corresponds to a horizontal path in the phase diagram that goes through the doublet GS region (see right diagram). Let us first consider the leftmost plot taken at magnetic field $B = 0$. On the left and right sides of this plot, the QD lies deep inside the singlet GS regime. Here the doublet ES approaches the superconducting gap edge, yielding an Andreev-level energy $\zeta \approx \Delta$. By moving to

* silvano.defranceschi@cea.fr

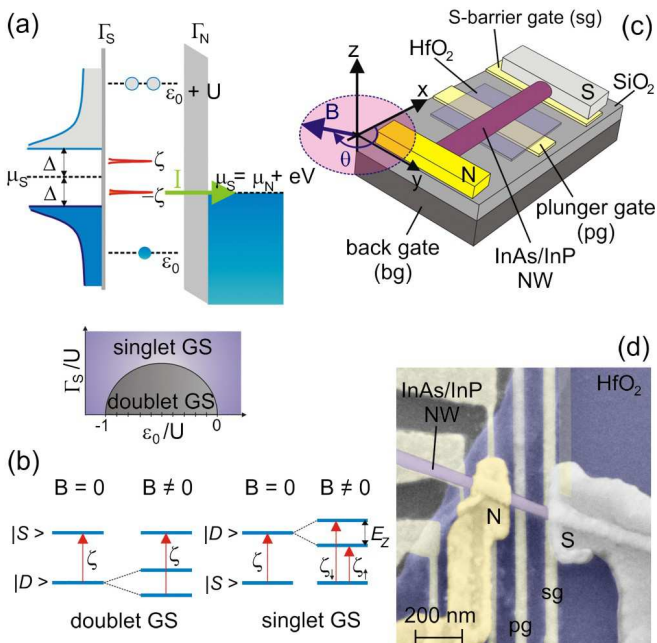


FIG. 1. Andreev levels in a hybrid S -QD- N system and device description. (a) (Upper panel) Schematics of a S -QD- N device with asymmetric tunnel couplings to the normal metal (Au) and superconductor (V) leads, Γ_N and Γ_S , respectively. Δ is the superconducting gap, U is the charging energy, μ_i is the chemical potential of the i lead, and ϵ_0 is the QD energy level relative to μ_S (in the $\Gamma_S \rightarrow 0$ limit, the QD has 0, 1 or 2 electrons for $\epsilon_0 > 0$, $-U < \epsilon_0 < 0$, $\epsilon_0 < -U$, respectively). The sub-gap peaks located at $\pm\zeta$ represent the Andreev levels. In tunnel spectroscopy measurements the alignment of μ_N to an Andreev level yields a peak in the differential conductance. (Lower panel) Qualitative phase diagram [9, 10, 13] depicting the stability of the magnetic doublet ($|D\rangle = |\uparrow\rangle, |\downarrow\rangle$) versus that of the BCS singlet ($|-\rangle$). (b) Low-energy excitations of the QD- S system and their expected evolution in a magnetic field, B . Doublet GS case (left): $|\uparrow\rangle$ is stabilized by B and Andreev levels related to the transition $|\uparrow\rangle \rightarrow |-\rangle$ are observed. Singlet GS case (right): at finite B , the excited spin-split states $|\uparrow\rangle$ and $|\downarrow\rangle$ give rise to distinct Andreev levels with energy ζ_\uparrow and ζ_\downarrow , respectively. $E_Z = |g|\mu_B B$ is the Zeeman energy, where $|g|$ is the g -factor and μ_B is the Bohr magneton. (c) Device schematic. The N and S leads were made of Ti(2.5 nm)/Au (50 nm) and Ti(2.5 nm)/V (45 nm)/Al (5 nm), respectively. The QD system is tuned by means of three gates: a plunger gate (pg), a barrier gate (sg) close to the S contact, and a back gate (bg). B is applied in the (x, y) device plane (x being parallel to the NW). (d) Scanning electron micrograph of a S -QD- N device.

towards the central region, the two sub-gap resonances approach each other and cross at the singlet-doublet phase boundaries, where $\zeta = 0$. In the doublet GS regime between the two crossings, the sub-gap resonances form a loop structure with ζ maximal at the electron-hole symmetry point. Increasing Γ_S corresponds to an upward shift in the phase diagram. The middle row in Fig. 2a refers to the case where Γ_S is just large enough to stabilize the singlet GS over the full V_{pg} range (see right

diagram). At $B = 0$, the Andreev levels approach the Fermi level without crossing it. A further increase in Γ_S leads to a robust stabilization of the singlet GS (bottom row). At zero-field, the sub-gap resonances remain distant from each other coming to a minimal separation at the electron-hole symmetry point ($\epsilon_0 = -U/2$). Similarly to the case of superconducting single-electron transistors [26], the QD occupation increases with V_{pg} in units of two without going through an intermediate odd state.

We now turn to the effect of B on the Andreev levels (middle and right columns in Fig. 2a). Starting from the weak coupling case (top row), a field-induced splitting of the sub-gap resonances appears, yet only in correspondence of a singlet GS. This is due to the fact that these resonances involve excitations between states of different parity. For a singlet GS, the spin degeneracy of the doublet ES is lifted by the Zeeman effect resulting in two distinct excitations (see Fig. 1b). By contrast, for a doublet GS, no sub-gap resonance stems from the $|\uparrow\rangle \rightarrow |\downarrow\rangle$ excitation, because these two states have the same (odd) number of electrons. The energy of the only visible Andreev level, associated with the $|\uparrow\rangle \rightarrow |-\rangle$ transition, increases with B . The formation of a loop structure in the rightmost panel of the middle row shows that a QPT from a singlet to a spin-polarized GS can be induced by B when the starting ζ is sufficiently small. In the bottom row, Zeeman-split Andreev levels can be seen all over the spanned V_{pg} range. At $B_x = 0.4$ T, the inner levels overlap at the Fermi level, indicating a degeneracy between the $|\uparrow\rangle$ and $|-\rangle$ states. In Fig. 2b we show theoretical dI/dV plots of a S -QD- N Anderson model calculated by means of self-consistent Hartree-Fock theory [27] (see Suppl. Material). The full phenomenology explained above is recovered, supporting our interpretation in terms of spin-resolved Andreev levels and a B field-induced QPT.

Interestingly, the splitting of Andreev levels appears to be gate dependent. It tends to vanish when the system is pushed deep into the singlet GS, and it is maximal near the phase boundaries. To further investigate this behaviour, we have measured $dI/dV(B, V)$ for fixed values of V_{pg} . These measurements were carried out on a second similar device (see Suppl. Material). The mid-panel of Fig. 3b displays the B_x dependence of the sub-gap resonances measured at position 1 in Fig. 3a. Initially, the energy of the Andreev levels increases, as expected for a doublet GS (see left panel). From a linear fit of the low-field regime, i.e. $\zeta(B_x) = \zeta(0) + E_Z/2$, where $E_Z = |g_x|\mu_B B_x$ is the Zeeman energy and μ_B is the Bohr magneton, we obtain a g -factor $|g_x| \approx 5.6$. For $B_x > 0.7$ T, the field-induced closing of the gap bends the Andreev levels down to zero-energy. Finally, above the critical field, a split Kondo resonance is observed, from which $|g_x| \approx 5.5$ is estimated, consistent with the value extracted from the Andreev level splitting. The mid-panel of Fig. 3c displays a similar measurement taken at position 2 in Fig. 3a, where the GS is a singlet. The splitting of the Andreev levels is clearly asymmetric. The lower energy level decreases to zero according to a

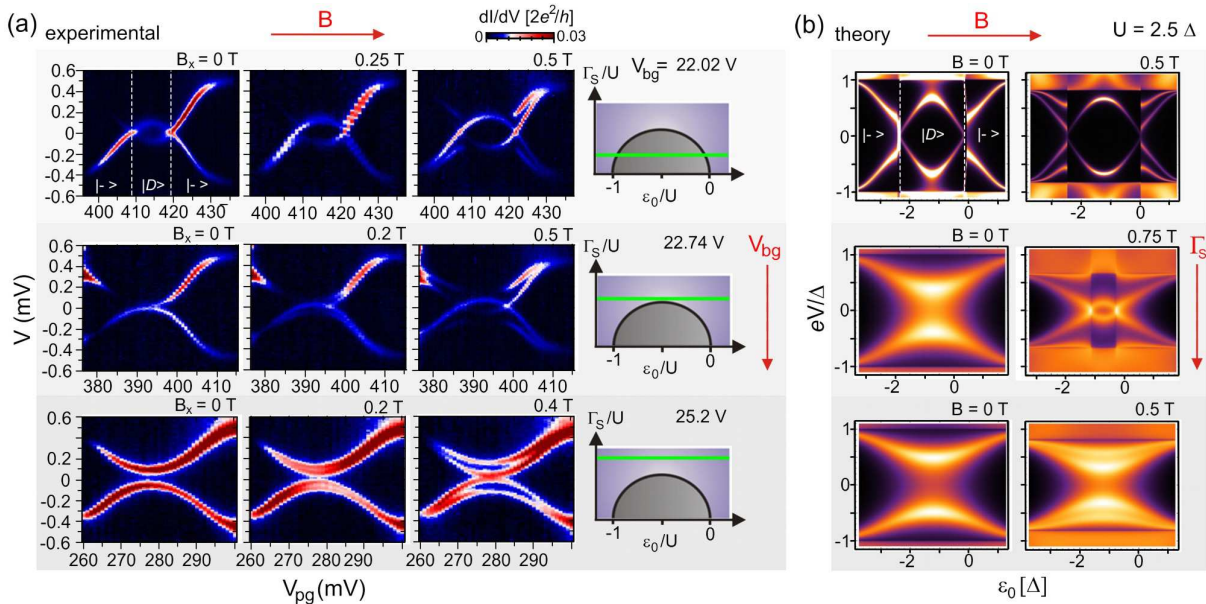


FIG. 2. **Andreev levels in different coupling regimes and their magnetic-field dependence.** (a) Experimental plots of dI/dV vs. (V_{pg}, V) for different QD-S couplings, Γ_S (increasing from top to bottom), and different B values (increasing from left to right). Top-left panel: along the V_{pg} range, the system GS changes from singlet ($|-\rangle$) to doublet ($|D\rangle$) and back to singlet, following the green trajectory in the qualitative diagram on the right side of the same row. We find that increasing V_{bg} results in larger Γ_S , thereby leading to an upward shift in the phase diagram. Eventually, the green trajectory is pushed into the singlet region (mid and bottom diagrams). Experimentally, this results in the disappearance of the doublet GS loop structure, as shown in the mid-left and bottom-left panels. The middle and right columns show the B -evolution of the Andreev levels in the three coupling regimes. For relatively weak coupling (top row), the Andreev levels for a singlet GS split due to the Zeeman effect, whereas those for a doublet GS simply move apart. At intermediate coupling (middle row), B induces a quantum-phase transition from a singlet to a spin-polarized GS, as denoted by the appearance of a loop structure (right panel). At the largest coupling (bottom row), the Zeeman splitting of the Andreev levels is clearly visible all over the V_{pg} range. The splitting is gate-dependent with a maximum in the central region. (b) Theoretical dI/dV plots calculated by means of a self-consistent Hartree-Fock theory. In all calculations we used $U = 2.5\Delta$ and $\Gamma_N/\Gamma_S = 1/3$. From top to bottom, Γ_S was set to 0.2Δ , 0.7Δ and 0.9Δ . In spite of the relative simplicity of the Anderson model, the full experimental phenomenology is recovered.

linear dependence $\zeta_{\uparrow}(B_x) = \zeta(0) - E_Z/2$, with $|g_x| \approx 6.1$, which is close to the value measured from the split Kondo resonance in the normal state. The higher energy level, however, exhibits a much weaker field dependence. Both the non-linear field dependence for $B_x > 0.7$ T in Fig. 3b and the asymmetric splitting in Fig. 3c can be explained in terms of a level-repulsion effect between the Andreev levels and the continuum of quasiparticle states. This interpretation is confirmed by numerical calculations shown in the right panels of Figs. 3b and 3c, which are in good agreement with the respective experimental data. In the mid-panel of Fig. 3c, the inner sub-gap resonances cross around 1.5 T, denoting a field-induced QPT. Above this field, however, they remain pinned as a zero-bias peak (ZBP) up to $B_c^x \approx 2$ T. This peculiar behavior, reproduced by the numerical results, can be attributed to the level-repulsion effect discussed above, in combination with the rapid shrinking of Δ with B_x .

In order to observe a clear B -induced QPT from a singlet to the spin-polarized GS, we reduced $\zeta(0)$ by tuning V_{pg} closer to the singlet-doublet crossing in Fig. 3a. The corresponding data are shown in Fig. 4a. Contrary to the case of Fig. 3c, the Andreev level splitting is rather symmetric, owing to the reduced importance of the level

repulsion effect at energies far from Δ . The inner sub-gap resonances split again after the QPT, which occurs now at $B_x \approx 0.5$ T. As expected, the outer sub-gap resonances get simultaneously suppressed (left panel of Fig. 3c). The suppression is not complete though, suggesting a partial population of the $|-\rangle$ ES, possibly favored by thermal activation.

We note that the ZBP at the QPT appears to extend on a sizable field range $\Delta B_x \approx 150$ mT. This range is consistent with the Γ_N -dominated lifetime broadening of the Andreev levels, i.e. $|g_x|\mu_B\Delta B_x \approx \text{peak width} \approx 50\mu\text{eV}$. In Fig. 4b we show how the ZBP depends on the in-plane B angle, θ , relative to the NW axis. As θ varies from 0 to $\pi/2$, the ZBP splits into two peaks with decreasing height. This angle dependence is an effect of the g -factor anisotropy. For $\theta = \pi/2$, we find a g -factor $|g_y| \approx 3$, i.e. a factor of 2 smaller than for $\theta = 0$ (see Suppl. Material). As a result, the QPT only occurs at a higher field (see Suppl. Material, $B_{QPT}^y \approx 1$ T), and the split peaks correspond to ζ_{\uparrow} transitions on the singlet-GS side. Figure 4b shows also a pair of small outer peaks associated with the ζ_{\downarrow} transitions. Their oscillatory position is as well due to g -factor anisotropy.

It is interesting to note that the B dependences dis-

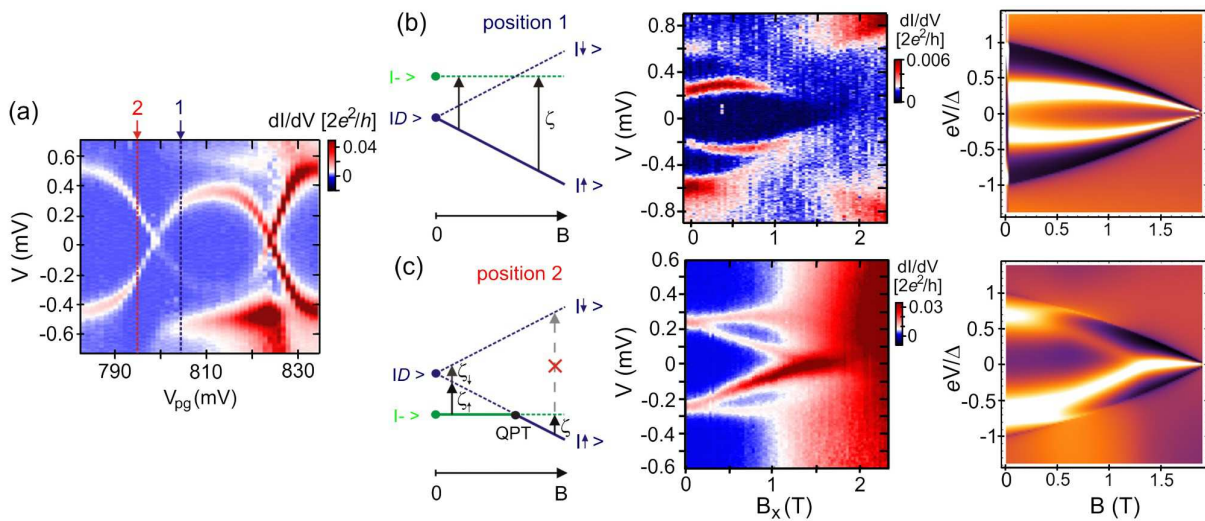


FIG. 3. **Magnetic-field evolution of the Andreev levels at fixed gate voltage and the level repulsion effect.** (a) $dI/dV(V_{pg}, V)$ measurement at $B = 0$ corresponding to a singlet-doublet-singlet sweep. (b) Left panel: Qualitative B -evolution of the low-energy states of a QD- S system as expected for a doublet GS. Middle panel: Corresponding experimental data measured at position 1 in (a). ζ increases linearly with B until it approaches the edge of the superconducting gap. The levels then move towards zero following the B suppression of Δ . Right panel: Corresponding theory plot of $dI/dV(B, eV/\Delta)$ calculated using experimentally measured parameters, i.e., $U/\Delta = 8$, $\epsilon_0/\Delta = -4$, and $\Gamma_S/\Delta = 1.5$ (Γ_N/Γ_S was set to $1/3$). (c) same as (b), but for singlet GS. The experimental plot in the middle panel was taken at position 2 in (a). It shows an asymmetric splitting of the ζ_+ and ζ_- peaks. The weak B dependence of ζ_- is due to the level repulsion between $|\downarrow\rangle$ and the continuum of quasiparticle states above Δ . The corresponding numerical results were taken with the same parameters as in (b), except $\epsilon_0/\Delta = -6$.

cussed above mimic some of the signatures expected for Majorana fermions in hybrid devices [16, 17, 28–30]. First, a ZBP is observed at finite B along the NW extending over a sizable field range. The peak splitting beyond the QPT resembles the energy splitting of Majorana states expected to occur for an increased coupling between neighbouring MFs resulting from the extended coherence length at higher fields [28–30]. Finally, the ZBP is suppressed for $\theta = \pi/2$, where B is presumably aligned to the Rashba spin-orbit field, B_{SO} [18, 19]. A closer inspection shows, however, that some of the QPT signatures differ from those expected from MFs. While Majorana ZBPs should occur only for fields perpendicular to B_{SO} , QPT-related ZBPs can be observed for any field direction, provided the field magnitude is adjusted to counterbalance g -factor anisotropies. Secondly, Majorana ZBPs are predicted to extend over larger field ranges, whereas the field extent of a QPT is limited by the ratio between the Andreev-level linewidth (which can be as low as the thermal energy in the small- Γ_N limit) and the g -factor. Figure 3b, however, shows that this latter limit can be overcome when the QPT occurs in concomitance with a closing superconducting gap. A similar stretching of the ZBP may also arise from nearby sub-gap states producing a level-repulsion effect on the inner

Andreev levels.

Methods

Device fabrication. The S -QD- N devices used in this study were based on individual InAs/InP core/shell nanowires grown by thermal evaporation [31] (diameter ≈ 30 nm, shell thickness ≈ 2 nm). The NWs were deposited onto Si/SiO₂ substrates on which arrays of thin metallic striplines [Ti(2.5 nm)/Au(15 nm), width ≈ 50 nm] covered by a 8 nm-thick atomic layer deposition (ALD) HfO₂ film had been previously processed. During the measurements, the degenerately-doped Si substrate was used as a global backgate, whereas the striplines were used as local gates. Normal metal [Ti(2.5 nm)/Au(50 nm)] and superconductor [Ti(2.5 nm)/V(45 nm)/Al(5 nm)] leads were incorporated to the devices by means of standard e-beam lithography techniques (lateral separation ≈ 200 nm).

This work was supported by the European Starting Grant program and by the Agence Nationale de la Recherche. R. A. acknowledges support from the Spanish Ministry of Economy and Innovation through grants FIS2009-08744 and FIS2012-33521. The authors thank J.-D. Pillet for useful discussions.

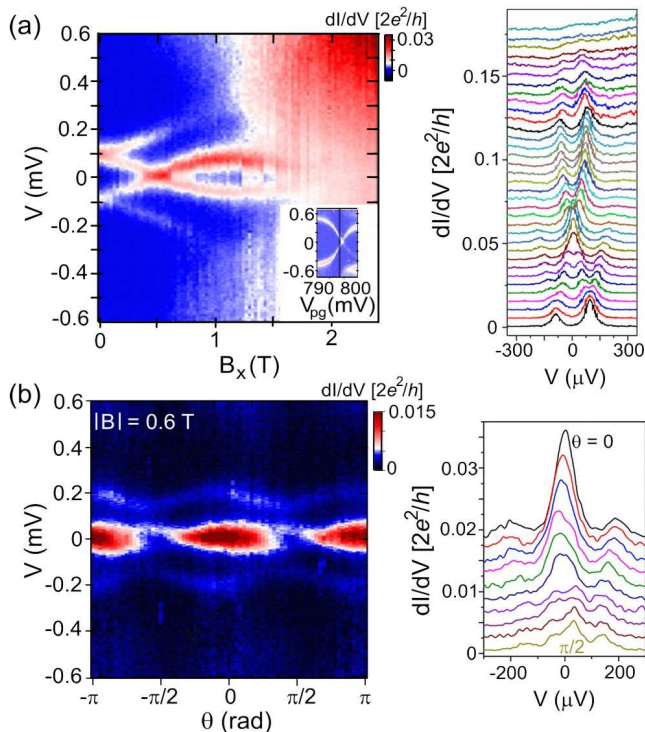


FIG. 4. **Magnetic-field induced QPT and angle anisotropy.** (a) Left panel: $dI/dV(B, V)$ taken at the position of the vertical line in the inset (same device as in Fig. 3). Right panel: line traces at equally spaced B values as extracted from the data in the left panel (each shifted by $0.005 \times 2e^2/h$). The QPT induced by the field is observed as a ZBP extending over a B range of about 150 mT. This apparently large extension is a consequence of the finite width of the Andreev levels. (b) $dI/dV(V)$ traces taken with $|B| = 0.6$ T, at different angles. This field magnitude corresponds to the QPT field when B is aligned to the NW axis at $\theta = 0$. Owing to the g -factor anisotropy, the ZBP associated with the QPT is split and suppressed when B is rotated away from the NW axis. The peak splitting has a maximum at $\theta = \pi/2$.

-
- [1] S. D. Franceschi, L. P. Kouwenhoven, C. Schonenberger, and W. Wernsdorfer, *Nature Nanotech.* **5**, 703 (2010).
- [2] A. Martín-Rodero and A. L. Yeyati, *Adv. Phys.* **60**, 899 (2011).
- [3] L. I. Glazman and K. Matveev, *JETP Lett.* **49**, 659 (1989).
- [4] J. A. van Dam, Y. V. Nazarov, E. P. A. M. Bakkers, S. D. Franceschi, and L. P. Kouwenhoven, *Nature* **442**, 667 (2006).
- [5] J. Cleuziou, W. Wernsdorfer, V. Bouchiat, T. Ondarochu, and M. Monthieux, *Nature Nanotech.* **1**, 53 (2006).
- [6] M. R. Buitelaar, T. Nussbaumer, and C. Schonenberger, *Phys. Rev. Lett.* **89**, 256801 (2002).
- [7] H. I. Jorgensen, T. Novotny, K. Grove-Rasmussen, K. Flensberg, and P. E. Lindelof, *Nano Lett.* **7**, 2441 (2007).
- [8] R. Maurand, T. Meng, E. Bonet, S. Florens, L. Marty, and W. Wernsdorfer, *Phys. Rev. X* **2**, 011009 (2012).
- [9] A. V. Rozhkov and D. P. Arovos, *Phys. Rev. Lett.* **82**, 2788 (1999).
- [10] E. Vecino, A. Martín-Rodero, and A. L. Yeyati, *Phys. Rev. B* **68**, 035105 (2003).
- [11] A. Oguri, Y. Tanaka, and A. C. Hewson, *J. Phys. Soc. Japan* **73**, 2494 (2004).
- [12] M. S. Choi, M. Lee, K. Kang, and W. Belzig, *Phys. Rev. B* **70**, 020502(R) (2004).
- [13] T. Meng, S. Florens, and P. Simon, *Phys. Rev. B* **79**, 224521 (2009).
- [14] A. Zazunov, V. S. Shumeiko, E. N. Bratus, J. Lantz, and G. Wendin, *Phys. Rev. Lett.* **90**, 087003 (2003).
- [15] N. M. Chtchelkatchev and Y. V. Nazarov, *Phys. Rev. Lett.* **90**, 226806 (2003).
- [16] R. M. Lutchyn, J. D. Sau, and S. D. Sarma, *Phys. Rev. Lett.* **105**, 077001 (2010).
- [17] Y. Oreg, G. Refael, and F. von Oppen, *Phys. Rev. Lett.* **105**, 177002 (2010).
- [18] V. Mourik, K. Zuo, S. M. Frolov, S. R. Plissard, E. P. A. M. Bakkers, and L. P. Kouwenhoven, *Science* **336**,

- 1003 (2012).
- [19] A. Das, Y. Ronen, Y. Most, Y. Oreg, M. Heiblum, and H. Shtrikman, *Nature Phys.* **8**, 887 (2012).
- [20] M. T. Deng, C. L. Yu, G. Y. Huang, M. Larsson, P. Caroff, and H. Q. Xu, *Nano Lett.* **12**, 6414 (2012).
- [21] R. S. Deacon, Y. Tanaka, A. Oiwa, R. Sakano, K. Yoshida, K. Shibata, K. Hirakawa, and S. Tarucha, *Phys. Rev. Lett.* **104**, 076805 (2010).
- [22] J. D. Pillet, C. H. L. Quay, P. Morfin, C. Bena, A. L. Yeyati, and P. Joyez, *Nature Phys.* **6**, 965 (2010).
- [23] T. Dirks, T. L. Hughes, S. Lal, B. Uchoa, Y. F. Chen, C. Chialvo, P. M. Goldbart, and N. Mason, *Nature Phys.* **7**, 386 (2011).
- [24] W. Chang, V. E. Manucharyan, T. S. Jespersen, J. Nygard, and C. M. Marcus, arXiv:1211.3954v1 (2012).
- [25] F. Giazotto, P. Spathis, S. Roddaro, S. Biswas, F. Taddei, M. Governale, and L. Sorba, *Nature Phys.* **7**, 857 (2011).
- [26] P. Lafarge, P. Joyez, D. Esteve, C. Urbina, and M. H. Devoret, *Nature* **365**, 422 (1993).
- [27] A. M. Rodero and A. L. Yeyati, arXiv:1209.3908v1 (2012).
- [28] E. Prada, P. San-Jose, and R. Aguado, *Phys. Rev. B* **86**, 180503(R) (2012).
- [29] D. Rainis, J. Klinovaja, and D. Loss, *Phys. Rev. B* **87**, 024515 (2013).
- [30] S. D. Sarma, J. D. Sau, and T. D. Stanescu, *Phys. Rev. B* **86**, 220506(R) (2012).
- [31] X. Jiang, Q. Xiong, F. Qian, Y. Li, and C. M. Lieber, *Nano Lett.* **7**, 3214 (2007).

Supplementary Information: Spin-resolved Andreev levels in hybrid superconductor-semiconductor nanostructures

Eduardo J. H. Lee¹, Xiaocheng Jiang², Manuel Houzet¹, Ramón

Aguado³, Charles M. Lieber², and Silvano De Franceschi¹

¹*SPSMS, CEA-INAC/UJF-Grenoble 1, 17 rue des Martyrs, 38054 Grenoble Cedex 9, France*

²*Harvard University, Department of Chemistry and Chemical Biology, Cambridge, MA, 02138, USA and*

³*Instituto de Ciencia de Materiales de Madrid (ICMM),*

Consejo Superior de Investigaciones Científicas (CSIC),

Sor Juana Inés de la Cruz 3, 28049 Madrid, Spain

Model and Hartree-Fock theory

As described in the main text, our nanowires are well described by a single-level quantum dot with competing superconducting correlations and on-site Coulomb interactions. A minimal model for describing this experimental configuration is given by a single level Anderson model coupled to a superconducting reservoir with Hamiltonian $H_{QD-S} = H_S + H_T^S + H_{QD}$. Here, H_{QD} models the uncoupled quantum dot, and is given by

$$H_{QD} = \sum_{\sigma=\uparrow,\downarrow} \epsilon_{\sigma} d_{\sigma}^{\dagger} d_{\sigma} + U n_{\uparrow} n_{\downarrow}, \quad (1)$$

where d_{σ}^{\dagger} creates an electron with spin σ on the dot level located at ϵ_{σ} . In the presence of an external magnetic field B , spin-degeneracy is broken and the levels are given by $\epsilon_{\uparrow} = \epsilon_0 - \frac{1}{2}E_Z$ and $\epsilon_{\downarrow} = \epsilon_0 + \frac{1}{2}E_Z$ with $E_Z = g\mu_B B$, being the Zeeman energy. The second term in Eq. (1) describes the local Coulomb interaction for two electrons with opposite spin within the dot ($n_{\sigma} = d_{\sigma}^{\dagger} c_{\sigma}$), where U is the charging energy. H_S describes the uncoupled superconducting lead, modelled by a BCS Hamiltonian

$$H_S = \sum_{k_S\sigma} \xi_{k_S} c_{k_S\sigma}^{\dagger} c_{k_S\sigma} + \sum_{k_S} \left(\Delta c_{k_S\uparrow}^{\dagger} c_{-k_S\downarrow}^{\dagger} + \text{h.c.} \right), \quad (2)$$

where $\xi_{k_S} = \epsilon_{k_S} - \mu_S$ is referred with respect to the chemical potential at the superconducting reservoir μ_S and Δ is the superconducting order parameter. H_T^S describes the coupling between the QD level and the superconductor and has the form

$$H_T^S = \sum_{k_S\sigma} \left(V_{k_S} c_{k_S\sigma}^{\dagger} d_{\sigma} + \text{h.c.} \right).$$

This coupling to the superconducting lead is characterized by the parameter $\Gamma_S = \pi \sum_{k_S} |V_{k_S}|^2 \delta(\omega - \epsilon_{k_S})$. As described in the main text, the competition between the three energy scales U , Δ and Γ_S governs the ground state of the model which can be either a singlet or a doublet. Finally, the experimental setup includes a normal reservoir. We model this by adding two extra terms to the Hamiltonian such that the total model reads $H = H_N + H_T^N + H_{QD-S}$. The first term describes the normal reservoir and reads $H_N = \sum_{k_N,\sigma} \xi_{k_N} c_{k_N\sigma}^{\dagger} c_{k_N\sigma}$, where $c_{k_N\sigma}^{\dagger}$ creates an electron with spin σ at the single-particle energy level $\xi_{k_N} = \epsilon_{k_N} - \mu_N$, with μ_N being the chemical potential at the normal reservoir. The coupling to the normal lead is given by the term

$$H_T^N = \sum_{k_N\sigma} \left(V_{k_N} c_{k_N\sigma}^{\dagger} d_{\sigma} + \text{h.c.} \right),$$

which defines $\Gamma_N = \pi \sum_{k_N} |V_{k_N}|^2 \delta(\omega - \epsilon_{k_N})$.

All the relevant quantities for the experiment can be extracted from the QD Green's functions in Nambu space defined as $\hat{G}_{\sigma}^r(t, t') = -i\theta(t - t') \langle [\Psi_{\sigma}(t), \Psi_{\sigma}^{\dagger}(t')]_{+} \rangle$, where $\Psi_{\sigma} = (d_{\sigma} \ d_{-\sigma}^{\dagger})^T$. In frequency space, the QD Green's function can be formally written as $\hat{G}_{\sigma}^r(\omega)^{-1} = \hat{G}^{r,(0)}(\omega)^{-1} - \hat{\Sigma}_{\sigma}(\omega)$, where $\hat{G}^{r,(0)}(\omega)$ is the non-interacting dot Green's function in Nambu space and the self-energy $\hat{\Sigma}_{\sigma}$ takes into account both the coupling to the leads and the Coulomb interaction. Of course, the full problem cannot be exactly solved and one needs to resort to approximations. In the main text, we present calculations using a Hartree-Fock (HF) decoupling of the self-energy [1]. It has been demonstrated that such HF decoupling gives reliable results when benchmarked against more sophisticated methods

such as numerical renormalization group [2]. The HF selfenergy is obtained by considering the first order diagrams in the Coulomb interaction. Its diagonal components in Nambu space are given by $\Sigma_{11,\sigma}^{HF} = -\Sigma_{22,-\sigma}^{HF} = U\langle n_{-\sigma} \rangle$, where the spin-resolved occupations $\langle n_{\sigma} \rangle = -\frac{1}{\pi} \int d\omega \text{Im} G_{11,\sigma}^r(\omega)$ have to be calculated *self-consistently*. Importantly, also the anomalous self-energies $\Sigma_{12,\sigma}^{HF} = (\Sigma_{21,\sigma}^{HF})^* = -U\langle d_{\uparrow}d_{\downarrow} \rangle$ have to be taken into account. The explicit expression for $\hat{G}_{\sigma}^{r,HF}(\omega)$ reads

$$\hat{G}_{\sigma}^{r,HF}(\omega) = \frac{1}{D(\omega)} \begin{pmatrix} \omega + \epsilon_{-\sigma} + i\Gamma_N + \Gamma_S \frac{\omega}{\sqrt{\Delta^2 - \omega^2}} + U\langle n_{\sigma} \rangle & \Gamma_S \frac{\Delta}{\sqrt{\Delta^2 - \omega^2}} + U\langle d_{\uparrow}d_{\downarrow} \rangle \\ \Gamma_S \frac{\Delta}{\sqrt{\Delta^2 - \omega^2}} + U\langle d_{\downarrow}^{\dagger}d_{\uparrow}^{\dagger} \rangle & \omega - \epsilon_{\sigma} + i\Gamma_N + \Gamma_S \frac{\omega}{\sqrt{\Delta^2 - \omega^2}} - U\langle n_{-\sigma} \rangle \end{pmatrix}. \quad (3)$$

The Andreev level spectrum of the system is given by the roots of the determinant $D(\omega) \equiv \text{Det}[\hat{G}_{\sigma}^{r,HF}(\omega)^{-1}]$, namely by the solutions of

$$\begin{aligned} (\omega - \epsilon_{\sigma} + i\Gamma_N + \Gamma_S \frac{\omega}{\sqrt{\Delta^2 - \omega^2}} - U\langle n_{-\sigma} \rangle)(\omega + \epsilon_{-\sigma} + i\Gamma_N + \Gamma_S \frac{\omega}{\sqrt{\Delta^2 - \omega^2}} + U\langle n_{\sigma} \rangle) \\ - (\Gamma_S \frac{\Delta}{\sqrt{\Delta^2 - \omega^2}} + U\langle d_{\uparrow}d_{\downarrow} \rangle)(\Gamma_S \frac{\Delta}{\sqrt{\Delta^2 - \omega^2}} + U\langle d_{\downarrow}^{\dagger}d_{\uparrow}^{\dagger} \rangle) = 0. \end{aligned} \quad (4)$$

The QD spectral function is defined as $A(\omega) = -\frac{1}{\pi} \text{Im} \text{Tr}[\hat{G}_{\sigma}^{r,HF}(\omega)]$, where the trace includes both spin and Nambu degrees of freedom.

In practice, the results presented in the main text were obtained by discretizing the Fourier space in a finite mesh of size $N = 2^{18}$ with $\omega_i \in [-D, D]$ and cutoff $D = 25\Delta$. Starting from an initial effective mean-field solution $\Sigma_{11,\uparrow} = -\Sigma_{22,\downarrow} = \frac{U}{2}$ [3], we iterate the HF equations until good numerical convergence in the spin-resolved occupations is reached (as a criterium for good convergence, the iteration stops when the relative error between successive occupations in the iteration loop is less than 10^{-5}).

For a given bias voltage $eV = \mu_N - \mu_S$, the conductance across the system is given by $\mathcal{G} = dI/dV$, where the total current can be decomposed into Andreev and quasiparticle contributions, $I = I_A + I_Q$. For voltages $eV \leq \Delta$, the quasiparticle current is zero, $I_Q = 0$, and the only contribution comes from Andreev processes. The Andreev current reads

$$I_A = \frac{2e}{h} \int d\omega [f_N(\omega - V) - f_N(\omega + V)] T_A(\omega), \quad (5)$$

where the Andreev transmission, defined as

$$T_A(\omega) = 4\Gamma_N^2 \sum_{\sigma} |G_{12,\sigma}^{HF}(\omega)|^2, \quad (6)$$

describes processes in which an electron (hole) from the normal side is reflected as a hole (electron) while an extra Cooper pair is created on the superconducting side. For voltages above the gap, also the quasiparticle contribution is finite and is given by:

$$I_Q = \frac{2e}{h} \int d\omega [f_N(\omega - V) - f_S(\omega)] T_Q(\omega), \quad (7)$$

with a quasiparticle transmission defined as

$$T_Q(\omega) = 4\Gamma_N\Gamma_S\theta(|\omega| - \Delta) \frac{|\omega|}{\sqrt{\omega^2 - \Delta^2}} \sum_{\sigma} [|G_{11,\sigma}^{HF}(\omega)|^2 + |G_{12,\sigma}^{HF}(\omega)|^2 - \frac{2\Delta}{|\omega|} \text{Re}\{G_{11,\sigma}^{HF}(\omega)[G_{12,\sigma}^{HF}(\omega)]^*\}]. \quad (8)$$

This quasiparticle contribution consists of three processes: 1) conventional tunneling, 2) an electron (hole) in the normal side is converted into a hole (electron) excitation in the superconducting side (branch crossing [4]), and 3) quasiparticle transfer from the normal lead into the superconducting lead, while creating (or annihilating) a Cooper pair as an intermediate state.

Analytic model for energy level repulsion

Below we derive a simple expression which describes the level repulsion between the doublet states and the states in the continuum of the superconducting lead at small coupling $\Gamma_S \ll \Delta$, in the regions of gate voltage corresponding to a singlet ground state.

The Hamiltonian for the superconducting lead given by Eq. (2) can be diagonalized after a Bogoliubov transformation,

$$H_S = \sum_{k_S \sigma} \epsilon_{k_S} \gamma_{k_S \sigma}^\dagger \gamma_{k_S \sigma}, \quad (9)$$

where $\gamma_{k_S \sigma} = u_{k_S} c_{k_S \sigma} + \sigma v_{k_S} c_{-k_S - \sigma}^\dagger$ are the annihilation operators of Bogoliubov quasiparticles with energy $\epsilon_{k_S} = [\Delta^2 + \xi_{k_S}^2]^{1/2}$, and $u_{k_S}, v_{k_S} = [(1 \pm \xi_{k_S}/\epsilon_{k_S})/2]^{1/2}$ are the BCS coherence factors. The projection of the Hamiltonian H_{QD-S} to a subspace of states with energy close to Δ in the leads then reads

$$H_{QD-S} = \sum_{k_S \sigma} \left(\Delta + \frac{\xi_{k_S}^2}{2\Delta} \right) \gamma_{k_S \sigma}^\dagger \gamma_{k_S \sigma} + H_{QD} + \frac{1}{\sqrt{2}} \sum_{k_S} \left[V_{k_S} \left(\gamma_{k_S \sigma}^\dagger - \sigma \gamma_{k_S - \sigma} \right) d_\sigma + \text{h.c.} \right]. \quad (10)$$

The sums in the r.h.s of this equation are restricted to momenta such that $|\xi_{k_S}| \ll \Delta$, and $u_{k_S}, v_{k_S} \approx 1/\sqrt{2}$.

At vanishing tunnel coupling, the ground state at $\epsilon_\uparrow > 0$ is the product state of the BCS ground state in the lead and the empty level in the dot, which we denote $|\emptyset\rangle$. Lowest energy excited states consist of the singly occupied level, $d_\sigma^\dagger |\emptyset\rangle$, as well as the BCS ground state filled with one Bogoliubov quasiparticle, $\gamma_{k_S \sigma}^\dagger |\emptyset\rangle$. When their energies ϵ_σ and ϵ_{k_S} are close and the tunnel couplings V_{k_S} are finite, the discrete state on the dot and the continuum of states in the leads hybridize. Then, we may use $|\Psi_\sigma\rangle = (A d_\sigma^\dagger + \sum_{k_S} B_{k_S} \gamma_{k_S \sigma}^\dagger) |\emptyset\rangle$ as a variational wavefunction for the excited states with spin σ . From the set of equations

$$(E - \epsilon_\sigma) A = \frac{1}{\sqrt{2}} \sum_{k_S} V_{k_S}^* B_{k_S}, \quad (11a)$$

$$\left(E - \Delta - \frac{\xi_{k_S}^2}{2\Delta} \right) B_{k_S} = \frac{1}{\sqrt{2}} V_{k_S} A, \quad (11b)$$

that determine possible eigenenergies E associated with the wavefunction $|\Psi_\sigma\rangle$, we obtain the following equation for the bound state excitation energy $\zeta_\sigma \approx E$ of state $|\sigma\rangle$:

$$\zeta_\sigma - \epsilon_\sigma = -\Gamma_S \sqrt{\Delta/[2(\Delta - \zeta_\sigma)]}. \quad (12)$$

It yields

$$\zeta_\sigma \simeq \begin{cases} \epsilon_\sigma - \Gamma_S \sqrt{\Delta/[2(\Delta - \epsilon_\sigma)]}, & \Delta - \epsilon_\sigma \gg (\Gamma_S^2 \Delta)^{1/3}, \\ \Delta - (\Gamma_S^2 \Delta/2)^{1/3}, & \epsilon_\sigma \simeq \Delta, \\ \Delta - \Gamma_S^2 \Delta/[2(\epsilon_\sigma - \Delta)^2], & \epsilon_\sigma - \Delta \gg (\Gamma_S^2 \Delta)^{1/3}. \end{cases} \quad (13)$$

Equation (13) describes the anticrossing (or level repulsion) between the dot state and the BCS continuum. Namely, a bound state forms at all values of ϵ_σ ; it gets closer to the edge of the BCS continuum – and the splitting $|\zeta_\downarrow - \zeta_\uparrow|$ vanishes – as ϵ_σ is increased. Note that the excitation energy of the bound state coincides with the Andreev level energy obtained from Eq. (4) at $\Gamma_S \ll \Delta$, in the regions near the edge of the continuum spectrum in the lead, where $\langle n_\uparrow \rangle = \langle n_\downarrow \rangle = 0$ and the last term in the l.h.s gives a negligible correction in $(\Gamma_S/\Delta)^{2/3} \ll 1$.

Similarly, when $\epsilon_{-\sigma}$ is close to $-(U + \Delta)$, and the dot is doubly occupied in the ground state $d_\uparrow^\dagger d_\downarrow^\dagger |\emptyset\rangle$ at vanishing tunnel coupling, we may use $|\Psi_\sigma\rangle = (A d_\sigma^\dagger + \sum_{k_S} B_{k_S} \gamma_{k_S \sigma}^\dagger d_\uparrow^\dagger d_\downarrow^\dagger) |\emptyset\rangle$ as a variational wavefunction at finite coupling and obtain the equation

$$\zeta_\sigma + \epsilon_{-\sigma} + U = -\Gamma_S \sqrt{\Delta/[2(\Delta - \zeta_\sigma)]}. \quad (14)$$

for $\zeta_\sigma \approx E - (2\epsilon + U)$. It is also in correspondence with Eq. (4) in the regions where $\langle n_\uparrow \rangle = \langle n_\downarrow \rangle = 1$.

Magnetic field dependence of Δ

The magnetic field dependence of the superconducting gap, Δ , was estimated from the dI/dV vs (B, V) measurement shown in Suppl. Fig. 1a, which was taken at the center of an even valley. As discussed in the main text, the Andreev levels appear at $eV \pm \Delta$ when the system lies deep inside the singlet GS. Thus, $\Delta(B)$ is readily obtained from the evolution of the sub-gap resonances as a function of B (Suppl. Fig. 1b). This experimental dependence was used for obtaining the theoretical dI/dV plots at finite B (shown in Figs. 2 and 3 of the main text).

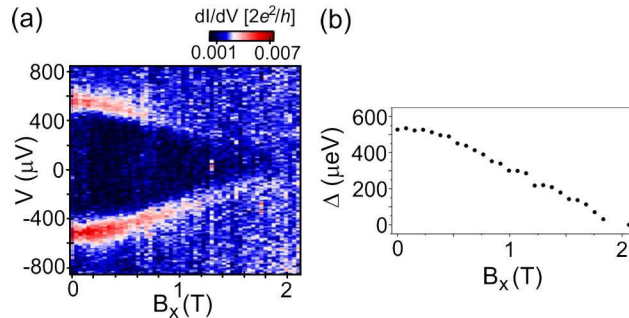


FIG. 1: (a) dI/dV vs. (B, V) measurement taken at the center of an even valley. (b) Superconducting gap extracted from (a) as a function of B_x .

Characterization of second S -QD- N device

Here we present additional data obtained from the device discussed in Figs. 3 and 4 of the main text. The device was first characterized in the normal state (Suppl. Fig. 2a). To this end, an external magnetic field $B = 2.5$ T was applied above the critical field $B_c \approx 2$ T, driving the vanadium electrical leads across the superconducting transition. The resulting charge stability diagram revealed a split Kondo resonance within the odd-occupied diamond (highlighted by the white arrows). Furthermore, a charging energy $U \approx 4.5$ meV is extracted from the height of the Coulomb diamond, whereas an average tunnel coupling $\langle \Gamma \rangle \approx 0.8$ meV is estimated from the FWHM of the Coulomb resonances.

The series of dI/dV vs. (V_{pg}, V) plots shown in Suppl. Fig. 2b ($B = 0, 0.5$ and 0.75 T) depicts the B -field evolution of the sub-gap Andreev levels in the second device. It is noteworthy that the data herein discussed shows a shift of ≈ 20 meV in the V_{pg} axis when compared to the corresponding plot in the main text (Fig. 3a). This can be attributed to a local charge rearrangement in the vicinity of the QD which, due to capacitive coupling, effectively results in a small shift of the charge stability diagram. In spite of the shift, the dI/dV features clearly remain unaltered. The data shown in Suppl. Fig. 2 is qualitatively analogous to the situation discussed in the top (experimental) row of Fig. 2 in the main text. Specifically, at $B = 0$ (left-most panel), the sub-gap resonances cross twice the Fermi level, delimiting the boundaries between the singlet (S) and doublet (D) ground states (GSs). In agreement with the discussion in the manuscript, the Andreev levels split with increasing magnetic field when the system lies in the singlet GS.

Supplementary data on energy level repulsion effect

Suppl. Fig. 3 contains further information concerning the energy level repulsion effect discussed in the manuscript. The right panel of Suppl. Fig. 3a displays an additional dI/dV vs (B, V) measurement taken at the position of the dashed line in the left panel, which is further away from the crossing point than position 2 in Fig. 3a of the main text. As discussed in the manuscript, the B -dependence of the ζ_{\downarrow} peaks deviates from the expected Zeeman splitting of the doublet state, due to the level repulsion of the $|\downarrow\rangle$ state by the continuum of quasiparticle states above the superconducting gap. Suppl. Fig. 3b demonstrates that this effect becomes more pronounced as the energy of the ζ_{\downarrow} peaks approaches Δ , as expected from theory. The plotted g -factor values were estimated from the slopes of the $\zeta_{\uparrow, \downarrow}$ vs. B data (red circles and blue triangles, respectively). The horizontal dashed line is positioned at $g \approx 5.5$, corresponding to the value estimated from the inelastic cotunneling dI/dV steps in the normal state (shown in Suppl. Fig. 3c). By its turn, the vertical dashed line signals the position of the singlet-doublet phase boundary. The plot

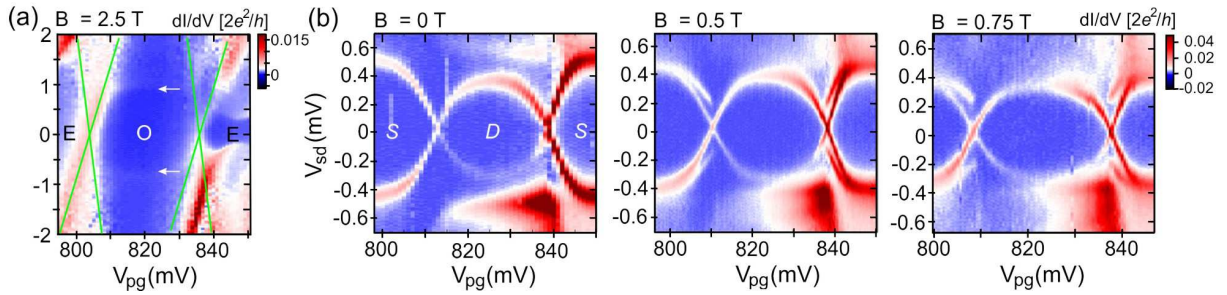


FIG. 2: (a) Characterization of second device in the normal state ($B = 2.5$ T). The green lines are guides to the eye depicting the limits of the Coulomb diamonds with even (E) and odd (O) occupation. The white arrows highlight inelastic cotunneling steps in dI/dV related to the split Kondo resonance. (b) Effect of B on the Andreev levels observed in the same device. A series of dI/dV vs (V_{pg}, V) plots taken at $B = 0, 0.5$ and 0.75 T is shown. S and D indicate the regions in which the ground state is a singlet or a doublet, respectively.

clearly shows how the g -factor extracted from the ζ_{\downarrow} peaks is strongly suppressed when moving away from the crossing point. The values obtained from the ζ_{\uparrow} peaks, on the other hand, show no significant plunger gate dependence.

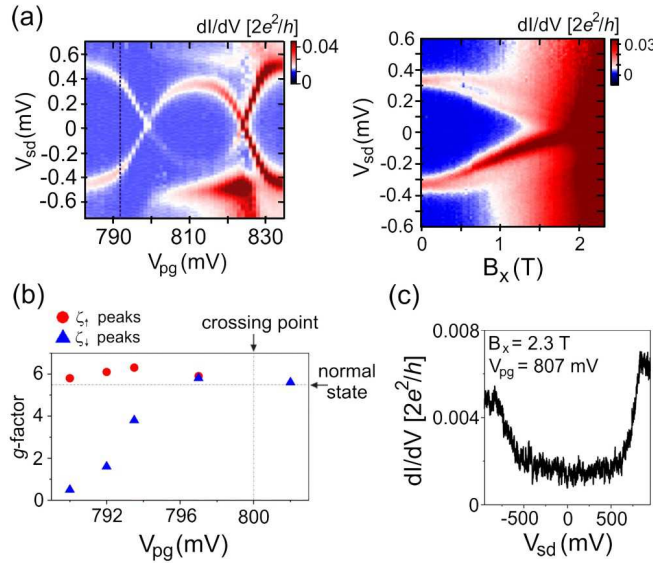


FIG. 3: (a) Right panel: dI/dV vs. (B, V) plot taken at the position marked by the dashed line in the left panel. The measurement shown in the left panel is the same as that shown in Fig. 3a in the main text. (b) g -factor estimated from ζ_{\uparrow} and ζ_{\downarrow} peaks as a function of V_{pg} . The level repulsion effect is evidenced by the suppressed ζ_{\downarrow} g -factor at positions further away from the crossing point, where the ζ_{\downarrow} peak energy approaches Δ . (c) Inelastic cotunneling dI/dV steps resulting from the field-induced splitting of a spin-1/2 Kondo resonance. This measurement, taken at $B = 2.3$ T, yields a normal state $g \approx 5.5$.

Supplementary data on angular dependence of the Andreev levels at finite B

To complement the angular dependence data shown in Fig. 4b of the main text, we include here the complete B -field dependences measured at $\theta = 0, \pi/2$ (Suppl. Fig. 4a). The plot shown in the left panel ($\theta = 0$) is analogous to the measurement shown in Fig. 4a of the main text. From this, a QPT field $B_{QPT}^x \approx 0.6$ T is estimated. The corresponding QPT measurement at $\theta = \pi/2$ (right panel) shows the same qualitative features, however with two significant differences. The most relevant difference is that the slope of the Andreev levels is reduced, indicating a smaller g -factor. This results in a QPT field $B_{QPT}^y > 1$ T. The g -factor anisotropy is highlighted in Suppl. Fig. 4b, where the data points were extracted from the angular dependence of ζ_{\uparrow} and ζ_{\downarrow} at a field magnitude $|B| = 0.6$ T (data shown in Fig. 4b of the main text). The second difference between the two data plots in Suppl. Fig. 4a is in the value of the respective critical fields: $B_c^x \approx 2$ T against $B_c^x \approx 1.5$ T.

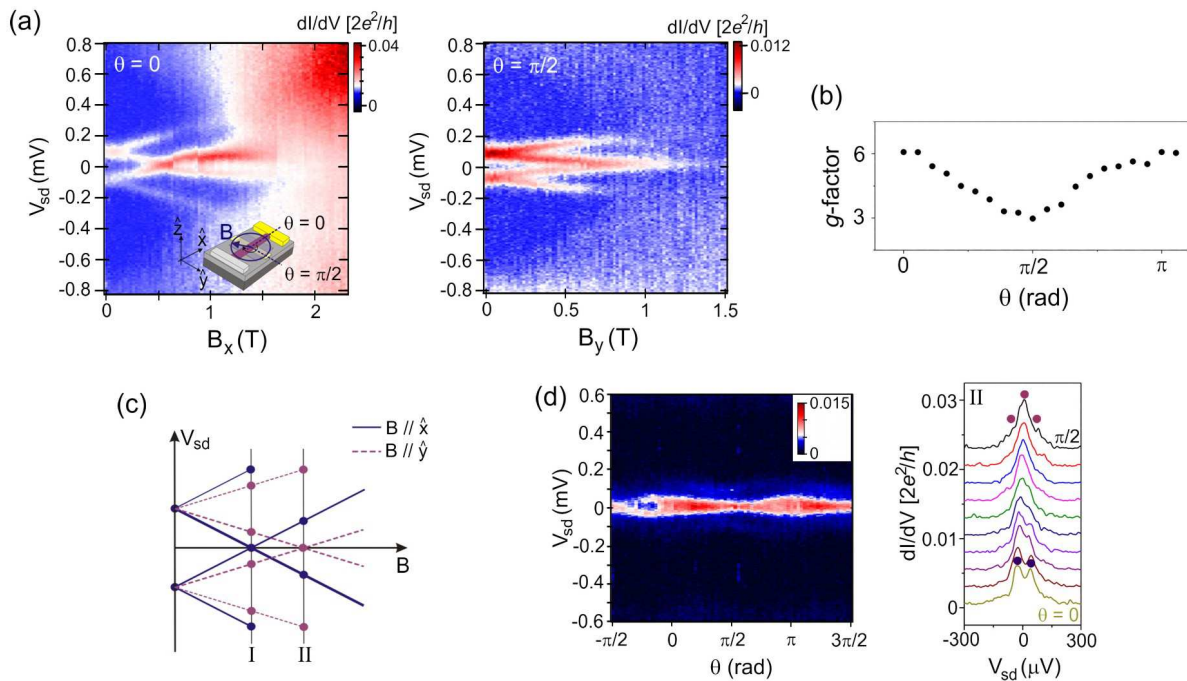


FIG. 4: (a) B -field dependences of the Andreev levels measured at $\theta = 0$ (left panel) and $\theta = \pi/2$ (right panel). The inset in the left panel shows the orientation of the field with respect to the nanowire ($\theta = 0$ corresponds to B aligned parallel to NW). (b) g -factor anisotropy measured from the Andreev level splitting at $|B| = 0.6$ T. (c) Schematic diagram summarizing the angular dependence behaviour. Due to the g -factor anisotropy, the QPT occurs at different fields for $\theta = 0$ (solid blue line) and $\pi/2$ (dashed violet line). Lines I and II highlight the dI/dV features observed when $|B|$ is fixed at $|B_{QPT}^x|$ and $|B_{QPT}^y|$, respectively. (d) Angular dependence measurement taken with $|B| = |B_{QPT}^y| = 0.35$ T. Here, the zero-bias QPT peak appears for B perpendicular to the nanowire axis. The circles in the line profile plot (right panel) ascribes the measured dI/dV peaks to the Andreev levels shown in (c).

The scheme depicted in Suppl. Fig. 4c summarizes the evolution of the Andreev levels for the longitudinal (solid line) and perpendicular (dashed line) field directions, as deduced from the data in panel (a). For a field amplitude $|B| = |B_{QPT}^x| = 0.6$ T, a zero-bias peak (ZBP) is observed at $\theta = 0$ (or $\theta = \pi$) in correspondence of the blue dot along line I. At $\theta = \pi/2$ (or $\theta = 3\pi/2$), the ZBP is split into two peaks in correspondence of the violet dots along line I. This is indeed the behaviour observed in Fig. 4b of the main text. The scenario is reversed when the field magnitude $|B|$ is fixed at $|B_{QPT}^y|$ (as indicated by line II). Unfortunately, the QPT in the perpendicular direction occurs near the closing of the gap (Suppl. Fig. 4a). To better visualize the angular dependence of the Andreev levels in the case $|B| = |B_{QPT}^y|$, the V_{pg} position was moved closer to the singlet-doublet phase boundary, so that the Andreev levels are closer to the Fermi level at $B = 0$. Suppl. Fig. 4d shows the angular dependence measurement taken at $|B| = 0.35$ T. In this case a ZBP is observed for $\theta = \pi/2$ (or $\theta = 3\pi/2$), in correspondence of the violet dot along line II, while a split peak is observed for $\theta = 0$ (or $\theta = \pi$), as denoted by the pair of blue dots along line II.

References

-
- [1] E. Vecino, A. Martín-Rodero and A. Levy Yeyati, *Phys. Rev. B* **68** 035105 (2003)
 - [2] A. Martín-Rodero and A. Levy Yeyati, *J. Phys. C* **24** 385303 (2012).
 - [3] J. D. Pillet, C. H. L. Quay, P. Morfin, C. Bena, A. Levy Yeyati and P. Joyez, *Nature Phys.* **6** 965 (2010).
 - [4] G.E. Blonder, M. Tinkham and T.M. Klapwijk, *Phys. Rev B* **25**, 4515 (1982).